CrossMark

JM PAPERS

Modelling the induction, thrust and power of a yaw-misaligned actuator disk

K.S. Heck[1], H.M. Johlas[1] and M.F. Howland[1],†

[1]Civil and Environmental Engineering, Massachusetts Institute of Technology, Cambridge, MA 02139, USA

Collective wind farm flow control, where wind turbines are operated in an individually suboptimal strategy to benefit the aggregate farm, has demonstrated potential to reduce wake interactions and increase farm energy production. However, existing wake models used for flow control often estimate the thrust and power of yaw-misaligned turbines using simplified empirical expressions that require expensive calibration data and do not extrapolate accurately between turbine models. The thrust, wake velocity deficit, wake deflection and power of a yawed wind turbine depend on its induced velocity. Here, we extend classical one-dimensional momentum theory to model the induction of a yaw-misaligned actuator disk. Analytical expressions for the induction, thrust, initial wake velocities and power are developed as a function of the yaw angle (γ) and thrust coefficient. The analytical model is validated against large eddy simulations of a yawed actuator disk. Because the induction depends on the yaw and thrust coefficient, the power generated by a yawed actuator disk will always be greater than a $\cos^3(\gamma)$ model suggests. The power lost due to yaw misalignment depends on the thrust coefficient. An analytical expression for the thrust coefficient that maximizes power, depending on the yaw, is developed and validated. Finally, using the developed induction model as an initial condition for a turbulent far-wake model, we demonstrate how combining wake steering and thrust (induction) control can increase array power, compared to either independent steering or induction control, due to the joint dependence of the induction on the thrust coefficient and yaw angle.

Key words: wakes, control theory

1. Introduction

Wake interactions between individual horizontal axis wind turbines can reduce wind farm energy production by 10–20 % (Barthelmie *et al.* 2009). Utility-scale wind turbines

† Email address for correspondence: mhowland@mit.edu

are controlled to maximize individual power production, rather than collective wind farm production (Boersma *et al.* 2017). Individual operation entails aligning each wind turbine in the farm with the incoming wind direction. In contrast, wake steering, where individual wind turbines are intentionally yaw-misaligned with respect to the incident wind direction, has emerged as a promising strategy to reduce wake interactions and increase collective wind farm power production (e.g. Gebraad *et al.* 2016; Bastankhah & Porté-Agel 2019; Kheirabadi & Nagamune 2019; Zong & Porté-Agel 2021; Howland *et al.* 2022*a*). Maximizing collective wind farm power production through wake steering control generally involves a trade-off between the power lost by the yaw-misaligned turbines and the power gained by the downwind-waked turbines, compared to standard individual control (e.g. Fleming *et al.* 2015). Since the power-maximizing yaw misalignment angles for wake steering control are estimated primarily using simplified analytical flow models (Gebraad *et al.* 2016; Fleming *et al.* 2019; Howland *et al.* 2022), it is important to accurately model the dependence of wind turbine power production and wake velocities on the yaw misalignment angle.

Wind turbine power production generally decreases as a function of an increasing yaw misalignment (γ) magnitude since the component of the wind velocity that is perpendicular to the rotor decreases. Textbooks instruct that the power production of a yawed wind turbine will decrease following $\cos^3(\gamma)$ (Burton *et al.* 2011). This estimate is based on the application of classical one-dimensional momentum theory with an incoming axial freestream wind speed $u_\infty \cos(\gamma)$ perpendicular to the rotor. However, wind turbines extract power from the winds at the rotor. The wind at the rotor is affected by the velocity induced by the wind turbine. Since the induction depends on the wind turbine thrust force, and the thrust force will decrease in yaw misalignment, the induction will depend on the yaw misalignment. The $\cos^3(\gamma)$ model neglects the dependence of the induction on the yaw misalignment (Micallef & Sant 2016). Given the error incurred by the $\cos^3(\gamma)$ model, most analytical wind farm power models assume that the power of a yaw-misaligned wind turbine follows $P_r(\gamma) = P(\gamma)/P(\gamma = 0) = \cos^{P_p}(\gamma)$, where P_p is an empirical, turbine-specific factor that needs to be tuned using experimental data (Dahlberg & Montgomerie 2005; Gebraad *et al.* 2016). However, such experiments are costly, since they require sustained operation of utility-scale wind turbines in suboptimal yaw misalignment angles (Howland *et al.* 2020*c*). Further, the wide spread in P_p values reported in the literature, typically $1 < P_p < 3$, suggests that the cosine model is not universal to different turbine models (Dahlberg & Montgomerie 2005; Schreiber *et al.* 2017; Liew, Urbán & Andersen 2020; Howland *et al.* 2020*c*). Accurate analytical predictions of $P_r(\gamma)$ remain an outstanding challenge (Hur *et al.* 2019) – as a starting point, in this study, we focus on analytical predictions of the induction and power production of yawed actuator disks.

Through analysis of an autogyro aircraft, Glauert (1926) developed an equation for the area-averaged induction and the coefficient of power as a function of the yaw misalignment γ. Glauert (1926) also identified that the induction of a yawed actuator disk varies over the rotor area about its mean value – this finding has been replicated in other actuator disk simulations and models (see review by Hur *et al.* 2019). Glauert's yawed actuator disk momentum theory is commonly used in blade-element momentum (BEM) models of rotational wind turbine aerodynamics (see e.g. review by Micallef & Sant 2016). Using the Bernoulli equation, Shapiro, Gayme & Meneveau (2018) proposed an equation for the dependence of the axial induction factor on the yaw misalignment of an actuator disk. Speakman *et al.* (2021) used the axial induction equation proposed by Shapiro *et al.* (2018) to model $P_r(\gamma)$ for a simulation with thrust coefficient 0.75, which yielded improved

power predictions compared to the $\cos^3(\gamma)$ model, but higher predictive error than a tuned $\cos^{P_p}(\gamma)$ with P_p set to 1.88.

Beyond modelling the power–yaw relationship (i.e. $P_r(\gamma)$), modelling the inviscid near-rotor wake region of a yawed actuator disk is important since inviscid models are often used as an initial condition for turbulent wake models that are used to predict wind farm power production (Frandsen *et al.* 2006; Bastankhah & Porté-Agel 2016; Shapiro *et al.* 2018). Therefore, it is equally important to accurately model the induction and the streamwise and spanwise velocity deficits at the outlet of the inviscid near-wake region for a yawed actuator disk.

Finally, a line of research parallel to wake steering has investigated methods for axial induction flow control, where individual wind turbines reduce the magnitude of their wind speed wake deficits by decreasing the thrust force (Annoni *et al.* 2016). A promising flow control methodology combines wake steering and induction control (Munters & Meyers 2018) – for such combined control, it is important to model the joint effect of the yaw misalignment and the wind turbine thrust coefficient on the power and wake deficit.

In this study, classical, inviscid momentum theory is extended to the yaw-misaligned actuator disk. Analytical expressions are developed for the rotor-normal induction, the streamwise velocity deficit, the spanwise velocity deficit, the thrust, and the power production of an actuator disk as a function of yaw misalignment. In § 2, a model is proposed based on a combination of momentum conservation, mass conservation and the Bernoulli equation. The model is validated against large eddy simulations (LES) of a yawed actuator disk. The numerical set-up of the LES is given in § 3, and results are provided in § 4. The model is validated against the LES in § 4.1. The dependence of the induction, velocity deficits and the power on the wind turbine thrust coefficient is presented in § 4.2. Further, in § 4.2 the model is optimized to find the thrust coefficient that maximizes power for each value of the yaw misalignment angle. In § 4.3, the induction model is used as an initial condition for a turbulent far-wake model. The implications of the developed induction–yaw model on quasi-steady wake steering and induction control are presented and discussed. Conclusions are provided in § 5.

2. Yawed actuator disk momentum theory

Our goal is to model the induction, thrust, wake deficit and deflection, and the power production of a yaw-misaligned actuator disk. For the following analysis, we assume that the flow is inviscid and frictionless. We assume that the velocity is continuous across the actuator disk, including both the streamwise and spanwise velocities, and that the pressure recovers to the incident freestream pressure away from the actuator disk. We note that the pressure recovery assumption is relevant to only the Bernoulli equation and streamwise momentum analysis. We do not apply this pressure recovery assumption to a lateral momentum balance, since it is well-known to introduce predictive error (Shapiro *et al.* 2018) due to counter-rotating vortices in the wake of yawed turbines (Howland *et al.* 2016). We consider uniform inflow (in y and z), as in standard momentum theory, and an actuator disk model (ADM) representation of the wind turbine forcing (Calaf, Meneveau & Meyers 2010; Burton *et al.* 2011). The ADM is introduced in § 2.1. The lateral velocity is modelled following lifting line theory (Shapiro *et al.* 2018) (§ 2.2). The induction is modelled by combining the Bernoulli equation, conservation of mass and momentum conservation to a control volume containing the yaw-misaligned actuator disk (§ 2.3). A schematic of the yaw-misaligned actuator disk and the control volume is shown in figure 1.
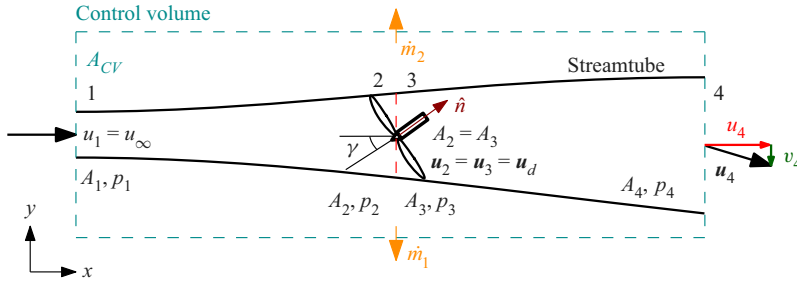
Figure 1. Control volume for the yawed actuator disk analysis. The streamwise and spanwise directions are x and y, respectively. The actuator-disk-modelled wind turbine is yaw-misaligned at angle γ, where positive yaw misalignment is a counter-clockwise rotation viewed from above. As in classical momentum theory, we consider four stations for the analysis, and the flow variables are labelled with the corresponding station numbers as subscripts. The cross-sectional areas, streamwise velocities, spanwise velocities, pressures and mass flow rates are denoted A, u, v, p and $\dot{m}$, respectively. The unit vector normal to the yawed actuator disk is shown as $\hat{n}$.

In § 2.3, we develop the equations to predict the induction, thrust, wake deficit and deflection, and the power production of a yaw-misaligned actuator disk. In § 2.4, we consider a limiting case of the developed induction model where the outlet spanwise velocity v_4 is negligible compared to the outlet streamwise velocity u_4, i.e. $|v_4| \ll u_4$.

2.1. *Actuator disk model*

The thrust force from an actuator disk on the surrounding flow depends on the freestream rotor-normal wind speed, $\boldsymbol{u}_\infty \cdot \hat{n}$:

$$\boldsymbol{F}_{T,ideal} = -\tfrac{1}{2}\rho C_T A_d (\boldsymbol{u}_\infty \cdot \hat{n})^2 \hat{n}, \tag{2.1}$$

where ρ is the density of the incident air, C_T is the coefficient of thrust, $A_d = \pi D^2/4$ is the area of the rotor disk, with D the wind turbine rotor diameter, $\hat{n}$ is the unit normal vector perpendicular to the disk, and $\boldsymbol{u}_\infty$ is the freestream wind velocity vector (Sørensen 2011). Wind turbines produce thrust and power based on the wind velocity at the rotor, which has been modified by induction. Thus the empirical thrust coefficient C_T depends on the induction. Additionally, for wind farms in the atmospheric boundary layer, it may be challenging to estimate the value of the freestream reference wind speed u_∞ due to wakes of upstream turbines or heterogeneity in the background flow field. Instead, an ADM is used to model wind turbine forcing, where the thrust force scales with the rotor-normal wind speed at the disk, $\boldsymbol{u}_d \cdot \hat{n}$, rather than the freestream $\boldsymbol{u}_\infty \cdot \hat{n}$ (Calaf *et al.* 2010). The ADM thrust force then depends on a modified thrust coefficient C_T' and the disk velocity (Calaf *et al.* 2010):

$$\boldsymbol{F}_T = -\tfrac{1}{2}\rho C_T' A_d (\boldsymbol{u}_d \cdot \hat{n})^2 \hat{n}. \tag{2.2}$$

Equation (2.2) is used in the ADM implementation in LES used for validation as well as the derivation of the analytical model.

Assuming that the freestream wind is uniform and aligned with the *x*-direction, the freestream wind vector is $\boldsymbol{u}_\infty = u_\infty \hat{\imath} + 0\hat{\jmath}$. In this study, we focus on uniform inflow, where the inflow wind $\boldsymbol{u}_\infty$ does not depend on y or z. This follows standard momentum theory (Burton *et al.* 2011), which avoids additional complexities in modelling turbine performance due to wind shear (Choukulkar *et al.* 2016; Howland *et al.* 2020c). However, the disk velocity may include a component in the *y*-direction for yaw-misaligned turbines,

and so is generally $\boldsymbol{u}_d = u_d \hat{\imath} + v_d \hat{\jmath}$. The rotor-normal, rotor-averaged induction factor a_n for a rotor with yaw misalignment angle γ is defined as

$$a_n = 1 - \frac{\boldsymbol{u}_d \cdot \hat{n}}{u_\infty \cos(\gamma)}. \tag{2.3}$$

In the yaw-aligned case where $\hat{n} = \hat{\imath}$, the rotor-normal induction factor a_n reduces to the standard (streamwise) axial induction factor $a = 1 - u_d/u_\infty$. The thrust force written in terms of the rotor-normal induction factor is then

$$\boldsymbol{F}_T = -\tfrac{1}{2}\rho C_T' A_d (1 - a_n)^2 \cos^2(\gamma)\, u_\infty^2 \left[\cos(\gamma)\, \hat{\imath} + \sin(\gamma)\, \hat{\jmath}\right]. \tag{2.4}$$

The power for the actuator disk is computed as $P = -\boldsymbol{F}_T \cdot \boldsymbol{u}_d$.

Rotational utility-scale wind turbines produce a thrust force that depends on the velocity at the turbine (e.g. Burton *et al.* 2011; Sørensen 2011; Howland *et al.* 2020*c*) – the velocity at the turbine is lower than u_∞ due to induction. Similarly, the ADM produces a thrust force that is proportional to the disk velocity, which has been modified by induction. The thrust force depends on the yaw misalignment for both utility-scale rotational wind turbines and the ADM. In the ADM, C_T' is an input. If we prescribe a value of C_T' that does not depend on the yaw angle, then the thrust force of the ADM depends on the yaw misalignment following $F_T(\gamma) \propto (1 - a_n)^2 \cos^2(\gamma)$. However, since the rotor-normal induction depends on the imposed thrust force F_T, and the thrust force decreases with an increasing magnitude of yaw misalignment, we hypothesize that the induction factor will depend on γ such that $a_n = a_n(\gamma)$.

The derivation in §§ 2.2 and 2.3 will prescribe an ADM-type forcing where C_T' is an input quantity. We emphasize that the proposed analytical model can be applied for a wind turbine model for which C_T' varies as a function of the yaw misalignment. This will be demonstrated in § 4.2.

In the model validation against LES in § 4.1, we compare the proposed model to an ADM forcing in LES where C_T' is a fixed quantity that does not depend on the yaw misalignment (see (2.2)). For different wind turbine models, a different form of the thrust force F_T may be appropriate (i.e. a form different to (2.2)). Specifically, C_T' may not be a fixed quantity, and would be a required, known input to the final model form. In general for rotational turbines, the potential dependence of C_T' on the yaw misalignment will depend on the turbine control strategy (i.e. the blade pitch and torque control) and the wind conditions (Howland *et al.* 2020*c*). For a different form of F_T, the quantitative model predictions would differ but the qualitative trends of the influence of yaw misalignment on the induction are expected to apply. Further discussion is included in Appendix E using wind tunnel data from Krogstad & Adaramola (2012), and the need for future work is highlighted in § 5.

2.2. *Lifting line spanwise velocity model with rotor-normal induction depending on yaw*

Yaw-misaligned wind turbines generate a counter-rotating vortex pair that deflects and deforms the wake region into a curled wake shape (Bastankhah & Porté-Agel 2016; Howland *et al.* 2016; Fleming *et al.* 2018; Martínez-Tossas *et al.* 2021). The counter-rotating vortex pair rotates about a low-pressure centre. Momentum balance approaches to predict the lateral velocity in the wake of a yaw-misaligned actuator disk that neglect the influence of the lateral pressure gradient often exhibit predictive errors (Jiménez, Crespo & Migoya 2010; Shapiro *et al.* 2018). Shapiro *et al.* (2018) developed a model for the spanwise velocity downwind of a yaw-misaligned actuator disk.

The approach uses Prandtl lifting line theory (Milne-Thomson 1973) to predict the spanwise velocity in the inviscid near-wake region downwind of the actuator disk. The downwash produced by the lifting line theory was presumed to be the spanwise velocity in the outlet of the streamtube enclosing the yawed actuator disk. The resulting model predicts the spanwise velocity disturbance $\delta v_0 = v_\infty - v_4 = \frac{1}{4} C_T u_\infty \cos^2(\gamma) \sin(\gamma)$. The model exhibited excellent predictions of the circulation at the disk hub-height ($z = 0$), defined as Γ_0 (Shapiro *et al.* 2018), over a range of yaw and thrust values. The spanwise velocity disturbance δv_0 was also compared to LES. The predictions exhibited improved accuracy compared to previous models, but had a slight underprediction of δv_0 at high yaw misalignment angles, $|\gamma| > 20°$ (Shapiro *et al.* 2018).

Following § 2.1, we consider the Prandtl lifting line approach developed by Shapiro *et al.* (2018) applied to the ADM with a prescribed C_T', instead of a prescribed C_T. The spanwise velocity disturbance is

$$\delta v_0 = v_\infty - v_4 = \frac{-\Gamma_0}{4R} = \frac{-\boldsymbol{F}_T \cdot \hat{\jmath}}{2\rho u_\infty A_d} = \frac{1}{4} \, C_T' u_\infty \sin(\gamma) \cos^2(\gamma) \, (1 - a_n(\gamma))^2 \,. \quad (2.5)$$

Comparing (2.5) to the model proposed by Shapiro *et al.* (2018), C_T' is the input quantity and there is an additional nonlinear dependence on $a_n(\gamma)$. We note that Shapiro *et al.* (2018) identified the influence of the yaw misalignment on the induction, and accounted for it by plotting δv_0 against C_T, where the thrust coefficient was estimated empirically as $C_T = C_T' \tilde{u}_d^2 / (u_\infty^2 \cos^2(\gamma))$, with $\tilde{u}_d$ the disk velocity measured from the LES validation case. In the following subsections, we will develop a predictive model for $a_n(\gamma)$ that uses (2.5).

2.3. *Model for the induction of a yaw-misaligned actuator disk*

To model the induction, we first apply the Bernoulli equation from stations 1 to 2 and from stations 3 to 4 within the streamtube, shown in figure 1:

$$\left.\begin{aligned} p_1 + \tfrac{1}{2}\rho\|\boldsymbol{u}_1\|^2 = p_2 + \tfrac{1}{2}\rho\|\boldsymbol{u}_2\|^2, \\ p_3 + \tfrac{1}{2}\rho\|\boldsymbol{u}_3\|^2 = p_4 + \tfrac{1}{2}\rho\|\boldsymbol{u}_4\|^2, \end{aligned}\right\} \quad (2.6)$$

where $\|\boldsymbol{u}_4\| = \sqrt{u_4^2 + v_4^2}$. We note that the outlet flow has non-zero components in the x ($\hat{\imath}$) and y ($\hat{\jmath}$) directions, denoted as u_4 and v_4, respectively (see figure 1). Assuming that the pressure recovers to the freestream at station 4 ($p_1 = p_4 = p_\infty$) and that the velocity across the rotor disk is continuous ($\boldsymbol{u}_2 = \boldsymbol{u}_3 = \boldsymbol{u}_d$), (2.6) can be combined and simplified to

$$p_2 - p_3 = \tfrac{1}{2}\rho \left(\|\boldsymbol{u}_1\|^2 - \|\boldsymbol{u}_4\|^2 \right). \quad (2.7)$$

Substituting in $\boldsymbol{u}_1 = \boldsymbol{u}_\infty$, $\boldsymbol{u}_4 = u_4\hat{\imath} + v_4\hat{\jmath}$ and $(p_2 - p_3)A_d = \|\boldsymbol{F}_T\|$, with $\boldsymbol{F}_T$ given by (2.4), this becomes

$$u_\infty^2 - u_4^2 - v_4^2 = C_T'(1 - a_n)^2 \cos^2(\gamma) \, u_\infty^2. \quad (2.8)$$

Next, we apply mass conservation to the streamtube between stations 2 and 4, where $A_2 = A_d$:

$$\boldsymbol{u}_4 \cdot (A_4\hat{\imath}) = \boldsymbol{u}_2 \cdot (A_2\hat{n}). \quad (2.9)$$

Substituting in $\boldsymbol{u}_2 = \boldsymbol{u}_d$ and the definition of a_n in (2.3), $\boldsymbol{u}_d \cdot \hat{n} = (1 - a_n)u_\infty \cos(\gamma)$, this simplifies to

$$u_4 A_4 = (1 - a_n)u_\infty \cos(\gamma) A_d. \tag{2.10}$$

We then apply mass conservation to the two-dimensional control volume, assuming that the flow outside the disk streamtube is unperturbed at u_∞:

$$\dot{m}_1 + \dot{m}_2 = \rho u_\infty A_{CV} - \rho u_\infty (A_{CV} - A_4) - \rho u_4 A_4$$
$$= \rho A_4 (u_\infty - u_4), \tag{2.11}$$

where *CV* denotes the control volume (figure 1). Finally, we apply conservation of momentum to the control volume in the streamwise direction ($\hat{\imath}$), using the Reynolds transport theorem assuming steady-state flow:

$$\rho \frac{\mathrm{D}u}{\mathrm{D}t} = \int_{CS} \rho u \, (\boldsymbol{u}_{rel} \cdot \mathrm{d}A) = \boldsymbol{F}_T \cdot \hat{\imath} + p_1 A_{CV} - p_4 A_{CV}, \tag{2.12}$$

where *CS* is the control surface. By expanding the surface integral and combining terms, this momentum balance simplifies to

$$\boldsymbol{F}_T \cdot \hat{\imath} = \rho u_4^2 A_4 - \rho u_\infty^2 A_4 + (\dot{m}_1 + \dot{m}_2)u_\infty. \tag{2.13}$$

Substituting (2.4), (2.10) and (2.11) into (2.13) and simplifying gives

$$-\tfrac{1}{2} C_T' u_\infty (1 - a_n) \cos^2(\gamma) = u_4 - u_\infty. \tag{2.14}$$

Finally, we solve for a_n in (2.8) from Bernoulli, u_4/u_∞ in (2.14) from conservation of mass and the streamwise momentum balance, and v_4/u_∞ in (2.5) from the lifting line spanwise velocity deficit model, resulting in a coupled nonlinear system of three equations to solve for $a_n(\gamma)$, $u_4(\gamma)$ and $v_4(\gamma)$:

$$\left. \begin{aligned} a_n(\gamma) &= 1 - \frac{\sqrt{u_\infty^2 - u_4(\gamma)^2 - v_4(\gamma)^2}}{\sqrt{C_T'} \, u_\infty \cos(\gamma)}, \\[2mm] \frac{u_4(\gamma)}{u_\infty} &= 1 - \tfrac{1}{2} C_T' \, (1 - a_n(\gamma)) \cos^2(\gamma), \\[2mm] \frac{v_4(\gamma)}{u_\infty} &= -\tfrac{1}{4} C_T' \, (1 - a_n(\gamma))^2 \sin(\gamma) \cos^2(\gamma). \end{aligned} \right\} \tag{2.15}$$

The system in (2.15) can be solved iteratively from an initial condition from standard, yaw-aligned momentum theory $a_n^0 = a = \tfrac{1}{2}(1 - \sqrt{1 - C_T}) = C_T'/(C_T' + 4)$ and typically converges in less than five iterations. While the system of equations in (2.15) converges quickly, it does not permit a straightforward solution. In § 2.4, we examine a limiting case of the model where the outlet spanwise velocity is neglected in the Bernoulli equation, $|v_4| \ll u_4$.

With a solution for the normal induction factor $a_n(\gamma)$ from (2.15), the power for a yaw-misaligned actuator disk is modelled as

$$P(\gamma) = -\boldsymbol{F}_T \cdot \boldsymbol{u}_d = \tfrac{1}{2} \rho C_T' A_d \, (1 - a_n(\gamma))^3 \, u_\infty^3 \cos^3(\gamma). \tag{2.16}$$

As discussed in the Introduction, the dependence of wind turbine power production on the yaw misalignment is often described by the power ratio $P_r(\gamma)$ (e.g. Howland *et al.* 2020*c*).

The resulting model for the power ratio is

$$P_r(\gamma) = \frac{P(\gamma)}{P(\gamma = 0)} = \left[\left(1 + \frac{1}{4} C_T' \right) (1 - a_n(\gamma)) \cos(\gamma) \right]^3, \qquad (2.17)$$

and the thrust ratio is

$$T_r(\gamma) = \frac{F_T(\gamma)}{F_T(\gamma = 0)} = \left[\left(1 + \frac{1}{4} C_T' \right) (1 - a_n(\gamma)) \cos(\gamma) \right]^2. \qquad (2.18)$$

Given the ADM turbine representation, the thrust force scales with the rotor-averaged disk velocity (e.g. Calaf *et al.* 2010). Therefore, the rotor-normal induction factor model in (2.15) is the prediction for the rotor-averaged induction factor, defined in (2.3) as a_n. Due to the yaw misalignment, the induction will also vary as a function of the azimuthal position about its rotor-averaged value (Glauert 1926). Glauert (1926) modelled this $\hat{a}_n(r, \theta) = \langle a_n(r, \theta) \rangle_A + a_n'(r, \theta)$, where $\hat{a}_n(r, \theta)$ is the rotor-normal induction depending on the radial r and azimuthal θ position, $\langle a_n(r, \theta) \rangle_A$ is the rotor-averaged induction (referred to as a_n elsewhere in the paper), and $a_n'(r, \theta)$ is the zero-mean, azimuthally dependent deviation from the rotor-averaged induction (Hur *et al.* 2019). The azimuthally dependent portion of the induction has been modelled empirically as $a_n'(r, \theta) = K_x(r/R) \sin(\theta)$, where R is the rotor radius, and K_x is an empirical factor (Glauert 1926; Hur *et al.* 2019). We note that $a_n'(r, \theta)$ averages to zero over the rotor $\left(\langle a_n'(r, \theta) \rangle_A = 0 \right)$. Since the ADM thrust ($F_T$) and power ($P$) depend on the rotor-averaged velocity, $a_n'(r, \theta)$ will not affect $a_n(\gamma)$, $F_T(\gamma)$ or $P(\gamma)$. For turbine models that apply thrust force unequally across the rotor, such as a blade-element (Howland *et al.* 2020*c*) or actuator line (Martínez-Tossas, Churchfield & Leonardi 2015) representation, $a_n'(r, \theta)$ can affect $F_T(\gamma)$ and $P(\gamma)$, and therefore must be modelled. We suggest future research on the radial and azimuthal variations of the rotor-normal induction factor for turbines beyond the ADM.

2.4. *Limiting case of CV analysis with $|v_4| \ll u_4$*

In this subsection, we consider the limiting case where the outlet spanwise velocity from the streamtube is significantly less than the outlet streamwise velocity, $|v_4| \ll u_4$. Therefore, the outlet velocity is $\|\boldsymbol{u}_4\| = u_4$. Starting from (2.15), the rotor-normal induction is simplified as

$$a_n(\gamma) = \frac{C_T' \cos^2(\gamma)}{4 + C_T' \cos^2(\gamma)}, \qquad (2.19)$$

which is also the induction factor reported by Shapiro *et al.* (2018), who assumed that the spanwise velocity disturbance appeared infinitesimally downwind of the yawed actuator disk and that it was constant in the streamtube downwind. The streamwise and spanwise velocities are

$$\frac{u_4(\gamma)}{u_\infty} = \frac{4 - C_T' \cos^2(\gamma)}{4 + C_T' \cos^2(\gamma)}, \qquad \frac{v_4(\gamma)}{u_\infty} = -\frac{4 C_T' \sin(\gamma) \cos^2(\gamma)}{(4 + C_T' \cos^2(\gamma))^2}. \qquad (2.20a,b)$$

The streamwise outlet velocity $u_4(\gamma)$ can also be written in terms of the induction factor $a_n(\gamma)$ such that $u_4(\gamma) = u_\infty(1 - 2a_n(\gamma))$, where $a_n(\gamma)$ is given by (2.19). This is analogous to the outlet velocity from one-dimensional momentum $u_4(\gamma = 0) = u_\infty(1 - 2a)$, where $a = a_n(\gamma = 0)$ is again the standard axial induction factor.

The power of the yawed actuator disk in this limiting case is

$$P(\gamma) = \frac{32\rho A_d C_T' \cos^3(\gamma)\, u_\infty^3}{(4 + C_T' \cos^2(\gamma))^3}. \tag{2.21}$$

The power and thrust ratios in this limiting case are

$$P_r(\gamma) = \left[\frac{(4 + C_T')\cos(\gamma)}{4 + C_T'\cos^2(\gamma)} \right]^3, \quad T_r(\gamma) = \left[\frac{(4 + C_T')\cos(\gamma)}{4 + C_T'\cos^2(\gamma)} \right]^2. \tag{2.22a,b}$$

The power ratio model given by (2.22a) was also reported by Speakman *et al.* (2021), who leveraged the streamwise induction model developed by Shapiro *et al.* (2018) (same as (2.19)).

3. Large eddy simulation numerical set-up

Large eddy simulations are performed using an incompressible flow code PadéOps (https://github.com/FPAL-Stanford-University/PadeOps; Ghate & Lele 2017; Howland, Ghate & Lele 2020a). Fourier collocation is used in the horizontal directions and a sixth-order staggered compact finite difference scheme is used in the vertical direction (Nagarajan, Lele & Ferziger 2003). Time advancement uses a fourth-order strong stability preserving variant of the Runge–Kutta scheme (Gottlieb, Ketcheson & Shu 2011), and the subgrid scale closure uses the sigma subfilter scale model (Nicoud *et al.* 2011).

The ADM is implemented with the regularization methodology introduced by Calaf *et al.* (2010) and further developed by Shapiro, Gayme & Meneveau (2019a). The ADM forcing depends on the prescribed input of C_T' (see (2.2)), which is varied independently of the yaw misalignment angle. The discretized turbine thrust force $\boldsymbol{f}(\boldsymbol{x})$ is distributed in the computational domain ($\boldsymbol{x}$) through an indicator function $\mathcal{R}(\boldsymbol{x})$ as

$$\boldsymbol{f}(\boldsymbol{x}) = \boldsymbol{F}_T\, \mathcal{R}(\boldsymbol{x}). \tag{3.1}$$

The thrust force $\boldsymbol{F}_T$ is computed with (2.2), depending on the disk velocity $\boldsymbol{u}_d$. The indicator function $\mathcal{R}(\boldsymbol{x})$ is constructed from a decomposition $\mathcal{R}(\boldsymbol{x}) = \mathcal{R}_1(x)\, \mathcal{R}_2(y, z)$ given by

$$\mathcal{R}_1(x) = \frac{1}{2s} \left[\mathrm{erf}\left(\frac{\sqrt{6}}{\Delta}\left(x + \frac{s}{2} \right) \right) - \mathrm{erf}\left(\frac{\sqrt{6}}{\Delta}\left(x - \frac{s}{2} \right) \right) \right], \tag{3.2}$$

$$\mathcal{R}_2(y, z) = \frac{4}{\pi D^2} \frac{6}{\pi \Delta^2} \iint H\left(\frac{D}{2} - \sqrt{y'^2 + z'^2} \right) \exp\left(-6\, \frac{(y - y')^2 + (z - z')^2}{\Delta^2} \right) \mathrm{d}y'\, \mathrm{d}z', \tag{3.3}$$

where $H(x)$ is the Heaviside function, $\mathrm{erf}(x)$ is the error function, s is the ADM disk thickness, and Δ is the ADM filter width. The disk velocity $\boldsymbol{u}_d$, used in the thrust force calculation (2.2), is calculated using the indicator function such that

$$\boldsymbol{u}_d = M \iiint \mathcal{R}(\boldsymbol{x})\, \boldsymbol{u}(\boldsymbol{x})\, \mathrm{d}^3 \boldsymbol{x}, \tag{3.4}$$

where $\boldsymbol{u}(\boldsymbol{x})$ is the filtered velocity in the LES domain, and M is an ADM filter width-dependent correction factor (Shapiro *et al.* 2019a). Depending on the numerical implementation of the indicator function, particularly the selection of ADM filter width

Δ, the ADM can underestimate the induction and therefore overestimate power production (Munters & Meyers 2017; Shapiro *et al.* 2019*a*). To alleviate this power overestimation for larger ADM filter widths, the disk velocity calculation in (3.4) uses a correction factor M derived by Shapiro *et al.* (2019*a*), which depends on C_T' and the ADM filter width. To compute the correction factor M, the Taylor series approximation for the ADM correction factor is used (Shapiro *et al.* 2019*a*) such that

$$M = \left(1 + \frac{C_T'}{4} \frac{1}{\sqrt{3\pi}} \frac{2\Delta}{D}\right)^{-1}. \tag{3.5}$$

The correction factor given by (3.5) was derived by Shapiro *et al.* (2019*a*) for yaw-aligned actuator disks. For low values of Δ/D, the correction factor M has a limited impact on the LES results, and the induction and power follow momentum theory (Shapiro *et al.* 2019*a*), but low ADM filter widths can also result in numerical oscillations in the flow field due to the ADM forcing discontinuity. For higher values of Δ/D with the correction factor implemented for a yaw-aligned ADM, the thrust force and power predicted by momentum theory are well reproduced, but the induced velocity in the LES domain does not conform to momentum theory due to the wide force smearing fundamental to the larger values of Δ/D (see Appendix A, figure 10). In the results presented in § 4 where analysis of the wake flow field is required, to reduce numerical oscillations in the wake, a larger ADM filter width $\Delta/D = 3h/(2D)$ is used with the correction factor M given by (3.5), where $h = (\Delta x^2 + \Delta y^2 + \Delta z^2)^{1/2}$. In the results presented in § 4 for which only the quantities at the actuator disk are analysed, a smaller ADM filter width of $\Delta/D = 0.29h/D = 0.032$ is used such that the correction factor is not required to reproduce the power predicted by momentum theory for the yaw-aligned ADM (see also the discussion by Shapiro *et al.* 2019*a*). In all cases, the ADM thickness is $s = 3\Delta x/2$. More discussion of the ADM numerical set-up and the interactions between the LES results and the ADM filter width and the correction factor is provided in Appendix A.

Consistent with the model derivation (see § 2), simulations are performed with uniform inflow with zero freestream turbulence. Periodic boundary conditions are used in the lateral y-direction. A fringe region (Nordström, Nordin & Henningson 1999) is used in the x-direction to force the inflow to the desired profile with a prescribed yaw angle. All simulations are performed with a domain $L_x = 25D$ in length, and cross-sectional size $L_y = 20D$, $L_z = 10D$, with $256 \times 512 \times 256$ grid points. A large cross-section is used to minimize the influence of blockage on the ADM, which changes as a function of turbine yaw. A single turbine is placed inside the domain at the centre of the y–z plane at a distance $5D$ from the domain inlet in the x-direction. Simulations are run for two flow-through times L_x/u_∞ to allow the turbine power output to converge, which is sufficient in these zero freestream turbulence inflow cases (Howland *et al.* 2016).

4. Results

In this section, the model predictions are compared to results from LES, and the model output is explored to reveal implications for wind farm flow control. In § 4.1, the predictive model developed in § 2 is validated against LES. The dependence of the induction on the coefficient of thrust is demonstrated in the model and in LES (§ 4.1). In § 4.2, the model is optimized to find the thrust coefficients that maximize the coefficient of power as a function of the yaw misalignment angle, and the predictions are compared to LES. Finally, in § 4.3, the model is used as an initial condition for a turbulent far-wake model.
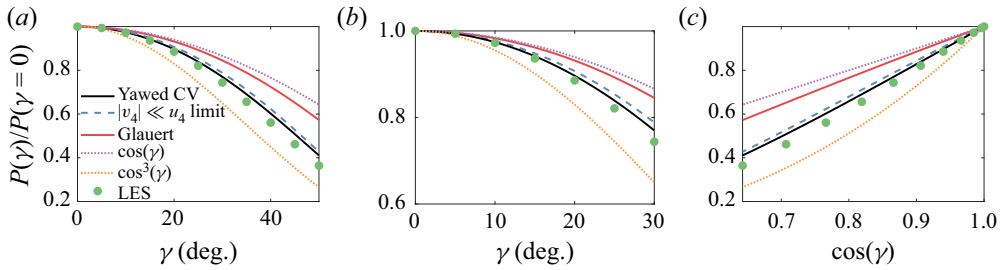
Figure 2. (*a*) Normalized power production for the yawed ADM wind turbine with $C'_T = 1.33$, normalized by the power production for a yaw-aligned ADM wind turbine ($P(\gamma)/P(\gamma = 0)$). The LES results are shown with green dots. The model predictions are given by the 'Yawed CV' curve, and the limiting case $|v_4| \ll u_4$ for the model is shown. For reference, $\cos^3(\gamma)$ and $\cos(\gamma)$ curves are shown in addition to the Glauert model (Appendix B). (*b*) Zoomed-in version of (*a*) to highlight the performance of different models. (*c*) Same as (*a*) with $\cos(\gamma)$ on the *x*-axis.

The influence of the induction–yaw relationship developed in § 2 on a wake steering test case is explored.

4.1. *Comparison between the model and LES*

The model for $P_r(\gamma)$ (2.17) is compared to LES in figure 2 for $C'_T = 1.33$ for yaw misalignments $0° \leqslant \gamma \leqslant 50°$. The model developed by Glauert (1926), with the functional form provided in Appendix B, and the developed model in the limit $|v_4| \ll u_4$ (§ 2.4) are also shown. Finally, $\cos(\gamma)$ and $\cos^3(\gamma)$ are shown for reference. The model developed in § 2.3 exhibits the lowest predictive error compared to the LES data. Neglecting the lateral velocity in the Bernoulli equation, $|v_4| \ll u_4$ (§ 2.4), results in a consistent overprediction of the power production at all yaw misalignment angles because the portion of momentum redistributed to the spanwise velocity, which does not contribute to power, is neglected. Neglecting the lateral velocity in the Bernoulli equation (2.7) increases the predicted pressure drop, and therefore the thrust force and the power, because the energy in the spanwise velocity is not accounted for in the outlet flow.

The Glauert model results in a larger power overprediction. This overprediction is expected, as discussed in Burton *et al.* (2011), since the lift contributions to the thrust in the Glauert model should not contribute to power because it does not contribute to net flow through the disk. The $\cos(\gamma)$ and $\cos^3(\gamma)$ curves provide upper and lower bounds, respectively, for the LES data and the model predictions. The commonly assumed $\cos^3(\gamma)$ model (Burton *et al.* 2011) underpredicts the power production because the yaw misalignment reduces the thrust force, which in turn reduces the rotor-normal induction and increases the disk velocity and the power production.

The model predictions and LES results for the rotor-normal induction $a_n(\gamma)$ are shown in figure 3. As with the power production, the most accurate predictions result from the yawed CV model in § 2.3. Assuming negligible lateral velocity (§ 2.4) results in an underprediction of the induction, which therefore results in an overprediction of the disk velocity and the power production (figure 2). The Glauert model overpredicts the induction, but also overpredicts the power, likely because of the lift contributions to thrust, as mentioned previously. We note that this is the Glauert model for the rotor-averaged induction. Therefore, the model for radial and azimuthal induction variations proposed by Glauert (1926) averages to zero (see § 2). The yawed CV model has increasing predictive error for the induction as a function of the yaw misalignment angle. This increasing
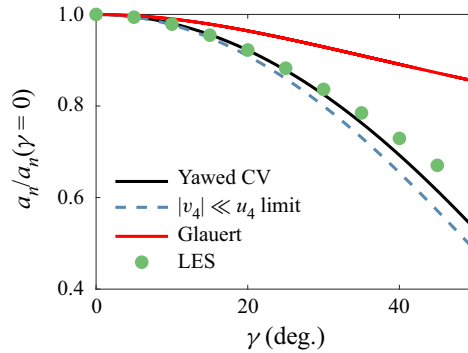
Figure 3. Normalized rotor-normal, rotor-averaged induction for the yawed ADM wind turbine with $C'_T = 1.33$. The model predictions are given by the 'Yawed CV' curve, and the limiting case $|v_4| \ll u_4$ for the model is shown. The Glauert model (Glauert 1926) for the rotor-averaged induction is provided in Appendix B.

error could be due to the assumption that the pressure recovers to freestream pressure downwind (see § 2), which was applied in the Bernoulli equation and in the streamwise momentum balance. The wake of a yaw-misaligned turbine curls due to the formation of a counter-rotating vortex pair (Howland *et al.* 2016). The counter-rotating vortex pair produces a low-pressure region in the yawed turbine wake that increases in magnitude, relative to the pressure drop at the rotor, with increasing turbine yaw (Shapiro *et al.* 2018), which is not modelled in the present framework. Future work should consider incorporating a pressure model in this framework.

The lateral velocity disturbance, $\delta v_0(\gamma) = v_\infty - v_4 = -v_4$, is estimated from LES by averaging the lateral velocity in cross-sections of the actuator disk streamtube (Shapiro *et al.* 2018). The lateral velocity disturbance $\delta v_0(\gamma)$, estimated as the maximum of the cross-sectional averages over x, is shown in figure 4(*a*) along with model predictions. The maximum value of the lateral velocity disturbance $\delta v_0(\gamma)$ generally occurs approximately $D/2$ downwind of the actuator disk wind turbine. The original C_T-based model of Shapiro *et al.* (2018) ($\delta v_0(\gamma) = \frac{1}{4}C_T u_\infty \cos^2(\gamma)\sin(\gamma)$) underpredicts the initial lateral velocity disturbance at higher yaw angles. The model developed here yields improved predictions compared to the original model by including the effect of the yaw misalignment on the induction, which the original expression based on C_T does not include. Since the induction decreases with increasing magnitude of the yaw angle, the disk velocity will increase. The increase in disk velocity increases the actuator disk thrust force, partially counteracting the reduction in thrust force from yaw misalignment. The lateral velocity disturbance based on C'_T and $a_n(\gamma)$ will therefore be larger than a prediction from a model that assumes a fixed C_T as a function of yaw γ.

Finally, the streamwise velocity disturbance is shown in figure 4(*b*). The LES streamwise velocity disturbance is estimated similarly to δv_0, although the maximum value of δu_0 generally occurs approximately $2D$ downwind of the actuator disk. The streamwise velocity disturbance associated with the yaw-aligned wind turbine, $\delta u_0/u_\infty = 2a(\gamma = 0)$, is shown as a reference. The streamwise velocity disturbance depends strongly on the yaw misalignment, therefore assuming $\delta u_0(\gamma \neq 0)/u_\infty = \delta u_0(\gamma = 0)/u_\infty = 2a(\gamma = 0)$ would yield significant predictive errors in a wake model. The full model (§ 2.3) has slightly improved predictions compared to the limit of negligible lateral velocity (§ 2.4), but both model estimates overpredict the streamwise velocity disturbance at larger yaw angles.
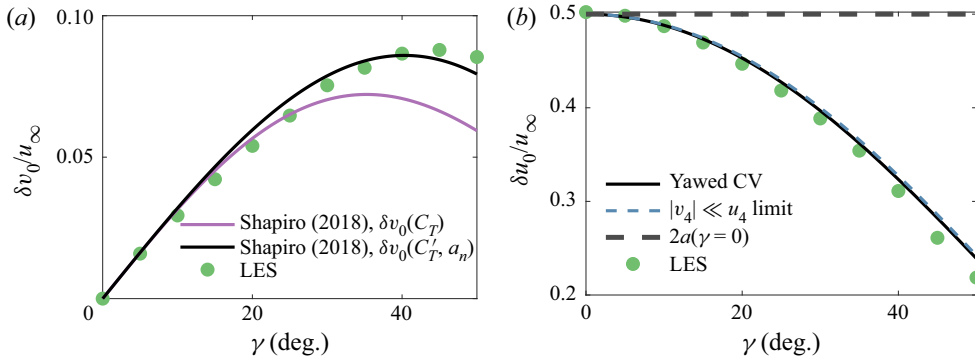
959 A9-12

Figure 4. (*a*) Normalized lateral velocity deficit with $C_T' = 1.33$. The model predictions for the lateral velocity depending on C_T are shown by $\delta v_0(C_T)$, where $C_T = 0.75$. The model predictions for the lateral velocity depending on the induction model given by (2.15) and C_T' are shown by $\delta v_0(C_T', a_n)$. (*b*) Normalized streamwise velocity deficit for the yawed ADM wind turbine with $C_T' = 1.33$. The model predictions are given by the 'Yawed CV' curve, and the limiting case $|v_4| \ll u_4$ for the model is shown.

The model developed in § 2 reveals that the induction a_n, the power P and the power ratio P_r all depend on both the yaw misalignment and the thrust coefficient C_T'. The ADM is simulated in LES over a range of yaw misalignment and C_T' values, where each pair (γ, C_T') represents a unique LES case. The influence of C_T' on the power ratio P_r for the LES data and the model (2.17) is shown in figure 5(*a*). The coefficient of power C_P is shown in figure 5(*b*). The model predictions exhibit low error, compared to the LES data, over a wide range of yaw and thrust values. We observe that the power reduction by yaw misalignment depends inherently on the value of C_T' (figure 5*a*), due to the influence of the thrust coefficient C_T' and yaw misalignment on the induction factor a_n (figure 5*c*). This result suggests that the power lost due to yaw misalignment in a practical field setting will be turbine-specific, since existing turbine designs operate at a wide range of thrust coefficients (see e.g. Hansen 2015). Further, since the thrust coefficient depends on the operating condition and turbine controller (e.g. Ainslie 1988), the power lost due to yaw misalignment will also vary in time for a given turbine design. Therefore, while an empirically tuned cosine model ($\cos^{P_p}(\gamma)$) may yield a sufficiently small error for a single turbine model and operating condition (e.g. region II operation; Pao & Johnson 2009), it cannot be expected to extrapolate to other wind turbine designs or control regimes. Instead, the physics-based model developed in § 2 can provide a prediction of $P_r(\gamma)$, provided that the thrust force characteristics (i.e. F_T or C_T') are known for the turbine model of interest as a function of yaw misalignment. Future work may integrate the induction–yaw model developed in § 2 into BEM codes (e.g. FAST; Jonkman & Buhl 2005).

4.2. *Optimizing model power and wake deflection in yaw misalignment with C_T'*

The induction and power models developed in § 2 and the results in § 4.1 indicate that the power production of a yaw-misaligned actuator disk depends on both the yaw misalignment and the local thrust coefficient C_T'. In yaw alignment, the well-known Betz limit result estimates that the axial induction factor that maximizes the coefficient of power $C_P = 2P/(\rho A_d u_\infty^3)$ is $a = 1/3$ (e.g. Burton *et al.* 2011), with a corresponding value of $C_T' = 2$. Here, we estimate the value of C_T' that maximizes C_P as a function of yaw misalignment value. The power produced by the actuator disk is given by (2.16). The maximum power occurs at $C_T'^*$ such that $\partial P / \partial C_T' = 0$. Taking the derivative of (2.16) with
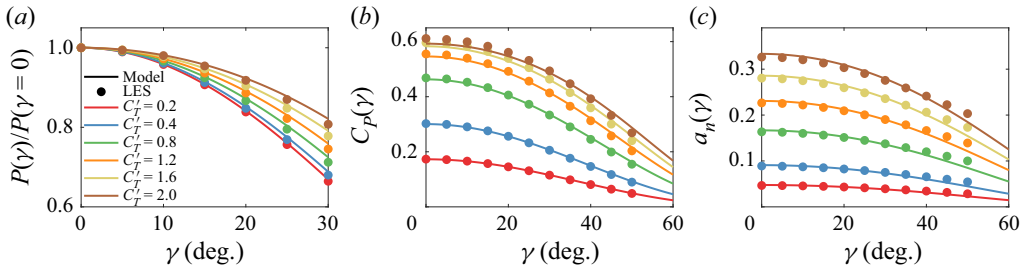
Figure 5. (*a*) Power production for the yawed ADM wind turbine, normalized by the power production for a yaw-aligned ADM wind turbine for various values of C'_T. (*b*) Coefficient of power $C_P(\gamma)$. (*c*) Rotor-normal, rotor-averaged induction factor $a_n(\gamma)$.

respect to C'_T yields

$$\frac{\partial P}{\partial C'_T} = \frac{1}{2}\,\rho A_d (1-a_n)^3 \cos^3(\gamma)\,u_\infty^3 - \frac{3}{2}\,\rho C'_T A_d (1-a_n)^2 \cos^3(\gamma)\,u_\infty^3\,\frac{\partial a_n}{\partial C'_T}. \qquad (4.1)$$

For the full model ((2.15), §2.3), $\partial a_n/\partial C'_T$ does not permit a straightforward analytical solution. To result in an analytical solution, we assume the limit $|v_4| \ll u_4$ (see §2.4), giving

$$\frac{\partial P}{\partial C'_T} = \frac{128\rho A_d \cos^3(\gamma)\,u_\infty^3}{(4 + C'_T \cos^2(\gamma))^4}\left[1 - \frac{1}{2}\,C'_T \cos^2(\gamma)\right], \qquad (4.2)$$

and power is maximized ($\partial P/\partial C'_T = 0$) at

$$C'^*_T(\gamma) = \frac{2}{\cos^2(\gamma)}. \qquad (4.3)$$

For yaw alignment ($\gamma = 0$), the standard Betz limit result is recovered with $C'^*_T(\gamma = 0) = 2$. For yaw misalignment ($\gamma \neq 0$), the power-maximizing thrust $C'^*_T(\gamma)$ increases monotonically as a function of increasing yaw misalignment magnitude. To maximize the power production of a yaw-misaligned wind turbine, the turbine should operate at a thrust coefficient different to the standard, optimal Betz value ($C_T = 8/9$, $a = 1/3$, $C'_T = 2$). The maximum power production as a function of the yaw misalignment is

$$P^*(\gamma) = \tfrac{8}{27}\rho A_d u_\infty^3 \cos(\gamma), \qquad (4.4)$$

and the maximum C_P as a function of the yaw misalignment is

$$C^*_P(\gamma) = \tfrac{16}{27}\cos(\gamma), \qquad (4.5)$$

which is equivalent to the Betz limit with an additional factor $\cos(\gamma)$. Therefore, subject to the assumptions discussed in §2, the minimum power production lost by a yaw-misaligned wind turbine is equal to $\cos(\gamma)$. As such, $\cos(\gamma)$ represents an upper bound for $P_r(\gamma)$ (figure 2) if C'_T is permitted to change.

The model predictions (2.15) for the coefficient of power C_P depending on the yaw misalignment and the thrust coefficient C'_T are shown in figure 6(*a*). Additionally, the optimal thrust coefficient $C'^*_T(\gamma)$, assuming $|v_4| \ll u_4$, is shown. The LES coefficient of power C_P, for the simulations with the disk velocity $\boldsymbol{u}_d$ correction M developed by Shapiro *et al.* (2019*a*) (3.5), is shown in figure 6(*b*). Figure 6(*c*) shows the same domain of input
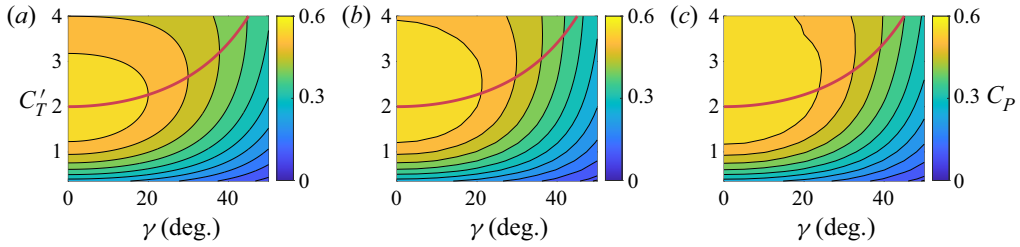
959 A9-14

Figure 6. (*a*) Coefficient of power $C_P = 2P(\gamma)/(\rho A_d u_\infty^3)$ as a function of the yaw misalignment γ and thrust coefficient C_T' estimated by the model given in (2.15) and (2.16). The values of C_T' that maximize power for each yaw misalignment angle are shown by the red line, given as $C_T'^*(\gamma) = 2/\cos^2(\gamma)$. (*b*) Same as (*a*) for LES C_P results, with the disk velocity correction factor M given by (3.5), and $\Delta/D = 3h/(2D)$. (*c*) Same as (*b*) for LES C_P results, with the disk velocity correction factor $M = 1$, and $\Delta/D = 0.29h/D = 0.032$.

yaw misalignment and C_T' for a low value of Δ/D with $M = 1$. Note that as numerical oscillations in the velocity field worsen with larger shear gradients at the boundary of the wake, the low Δ/D LES contours in figure 6(*c*) become less smooth (and accurate) as C_T', and therefore δu_0, increases. There are similar qualitative trends in the LES C_P compared to the model predictions in figure 6(*a*), especially for $C_T' \lesssim 2$. As demonstrated in figure 5, the model predicts the LES output quantitatively well. The differences between the model predictions and LES values of C_P generally increase with increasing C_T'. One cause of discrepancy, in addition to potential modelling simplifications in § 2, is that the ADM implementation in LES is known to underestimate wind turbine induction (Munters & Meyers 2017; Shapiro *et al.* 2019*a*). Consequently, the maximum coefficient of power in LES is $C_P = 0.60$, even with the correction factor used, which is higher than the Betz limit (0.593). Additionally, standard yaw-aligned momentum theory has increased error for heavily loaded turbines with high induction (Wilson & Lissaman 1974; Burton *et al.* 2011). The transition point to a heavily loaded rotor was approximated empirically by Wilson & Lissaman (1974) as $a \approx 0.37$ (corresponding to $C_T' \approx 2.32$). Therefore, increased error from momentum theory predictions for $C_T' \gtrsim 2.32$ are anticipated. This is discussed further in Appendix D.

Following a similar procedure, the thrust coefficient value that maximizes the magnitude initial lateral velocity $|v_4|$, and therefore the wake deflection, is $C_T'(\gamma) = 4/\cos^2(\gamma)$. However, these values of $C_T'(\gamma)$ produce inductions that are greater than 1, which is inconsistent with the momentum-theory-based model in (2.15). Therefore, for realizable values of C_T', the lateral velocity magnitude $|v_4|$ is a monotonically increasing function of C_T'. Conversely, u_4, the streamwise wake velocity, is a monotonically decreasing function of C_T'.

The model-predicted normalized streamwise and spanwise outlet velocities are shown in figures 7(*a*) and 7(*b*), respectively. While the power production reveals a non-monotonic trend and permits an optimal set of thrust coefficients ($C_T'^*(\gamma)$), both u_4 and $|v_4|$ show monotonic behaviour for realizable values of C_T'. For wake steering, the power production of a waked turbine will depend on both the streamwise wake velocity (u_4), and the wake deflection (integrated form of v_4). Notably, the wake deflection is an increasing function of C_T' (figure 7*a*), but the velocity deficit is also an increasing function of C_T' (figure 7*b*). Therefore, the value of C_T' that maximizes the power production of a waked downwind turbine will depend on the wind farm and flow configuration. In § 4.3, we explore this dependency in an analytical, turbulent wake model that uses the inviscid model developed in § 2 as an initial condition.
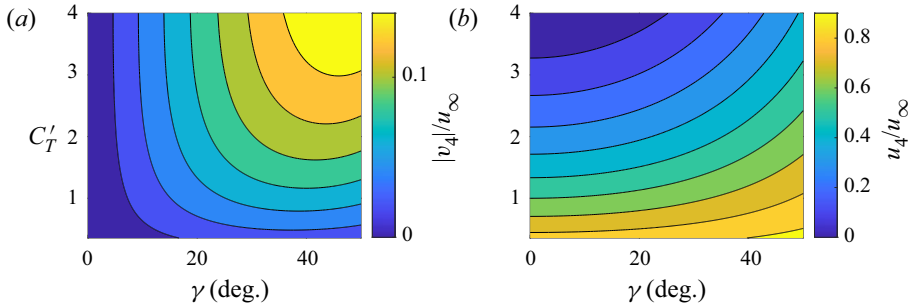
Figure 7. (a) Magnitude of the initial lateral velocity $|v_4|/u_\infty$ as a function of the yaw misalignment γ and thrust coefficient C_T' estimated by the model given in (2.15). (b) Initial streamwise velocity u_4/u_∞ as a function of the yaw misalignment γ and thrust coefficient C_T' estimated by the model given in (2.15).

4.3. *Implications for wake steering and induction control*

The impact of the yaw misalignment γ on the rotor-normal induction a_n will impact the power production, wake deflection and wake velocity deficit of a yaw-misaligned turbine. All three of these effects will modify the performance of wake steering control (intentional yaw misalignment). Similarly, as demonstrated in §§ 4.1 and 4.2, changing the local thrust coefficient C_T' (often called induction control) will also influence the power and wake properties of a yaw-misaligned turbine. In this subsection, we assess the role of yaw and thrust modifications on combined wake steering and induction flow control.

To assess the role of the developed induction model on wake steering and induction-based wind farm flow control, the model (see § 2, (2.15)) is used as an initial condition for a turbulent far-wake model. Inviscid near-wake models are commonly used as initial conditions for far-wake models (e.g. Frandsen *et al.* 2006; Bastankhah & Porté-Agel 2016; Shapiro *et al.* 2018). A Gaussian far-wake model is used, and the full model form is provided in Appendix C. The case study will seek to identify the pair of values for the thrust coefficient C_T' and the yaw misalignment γ that maximizes collective farm power production.

We consider a simplified wind turbine array with two wind turbines spaced with streamwise and spanwise separations $S_x = 8D$ and $S_y = 0.5D$, respectively. Given the spanwise spacing $S_y = 0.5D$, positive yaw misalignments (counter-clockwise rotation viewed from above) will be preferable to negative yaw (e.g. Howland *et al.* 2022). For illustrative purposes, the wake model parameters, which are the wake spreading rate and the proportionality constant of the presumed Gaussian wake, are set to representative values from the literature: $k_w = 0.07$ (Stevens, Gayme & Meneveau 2015; Howland *et al.* 2020b) and $\sigma_0 = 0.25$ (Shapiro *et al.* 2019b), respectively. We vary the yaw misalignment γ_1 and the thrust coefficient $C_{T,1}'$ of the leading freestream turbine. The yaw misalignment and thrust coefficient for the downwind turbine are held constant at the individual power-maximization levels $\gamma_2 = 0°$ and $C_{T,2}' = 2$, respectively. The set-up of the two-turbine collective control case study is shown in figure 8.

We consider the wind farm efficiency as a function of the yaw misalignment and the thrust coefficient of the leading turbine. The wind turbine efficiency η_i for turbine i is given by

$$\eta_i(\gamma_1, C_{T,1}') = \frac{P_i(\gamma_1, C_{T,1}')}{\frac{1}{2}\rho A_d u_\infty^3}. \tag{4.6}$$
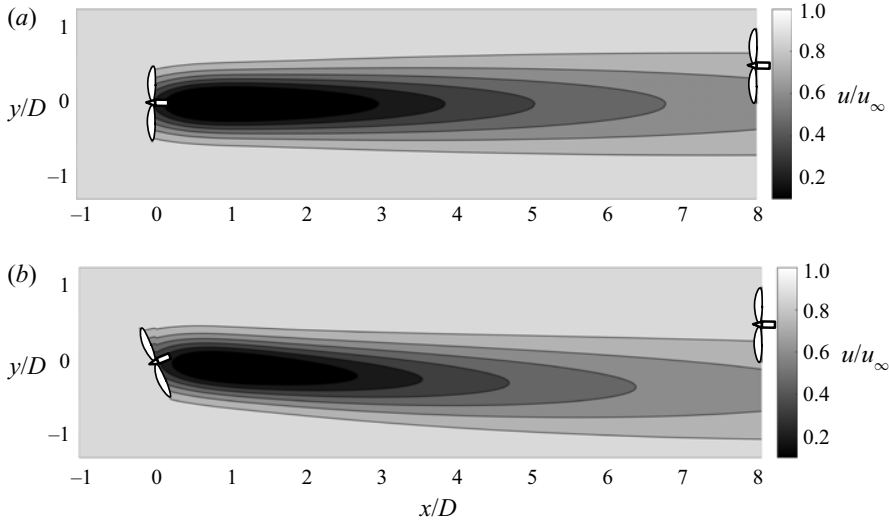
Figure 8. Collective wind farm control two-turbine case study. The turbines are spaced at $S_x/D = 8$ and $S_y/D = 0.5$ in the streamwise and spanwise directions, respectively. (*a*) Standard, individual turbine control with $C'_{T,1} = 2$ and $\gamma_1 = 0°$. (*b*) Model-optimal collective control with $C'_{T,1} = 2.11$ and $\gamma_1 = 24°$.

Equation (4.6), which is a non-dimensional representation of the power production, differs from C_P because it is based on the freestream wind speed u_∞ for both freestream and waked turbines.

The coefficient of power for a yawed actuator disk is $C_P = 2P/(\rho A_d u_\infty^3) = C'_T (1 - a_n(\gamma))^3 \cos^3(\gamma)$. The power production of each turbine is estimated as

$$P_i(\gamma) = \tfrac{1}{2}\rho C'_{T,i} A_d \left[(1 - a_{n,i}(\gamma_i, C'_{T,i})) \cos(\gamma_i) \, u_{e,i} \right]^3, \tag{4.7}$$

where u_e is the rotor-averaged velocity accounting for wake interactions (more details are provided in Appendix C). The wind farm efficiency is $\eta = \sum_{i=1}^{N_t} \eta_i / N_t$, where N_t is the number of wind turbines.

The total wind turbine array efficiency η is shown as a function of γ_1 and $C'_{T,1}$ in figure 9(*a*), with the array efficiency-maximizing point denoted with the star symbol. We can make a few observations. First, we note that the maximum array efficiency does not occur at $\gamma_1 = 0°$ and $C'_{T,1} = 2$, the optimal settings for an individual turbine, meaning that the array efficiency can be increased through flow control. The array efficiency maximizing value of $C'_{T,1}$ at each yaw misalignment value is shown by a dashed line in figure 9(*a*).

Second, the maximum array efficiency is also not located directly on the individual turbine C_P maximizing curve (see § 4.2) of $C'^*_{T,1}(\gamma_1) = 2/\cos^2(\gamma_1)$. In particular, the array efficiency-maximizing values of $C'_{T,1}$ are always below the turbine 1 efficiency-maximizing values given by $C'^*_{T,1}(\gamma_1) = 2/\cos^2(\gamma_1)$. At low yaw misalignment values, the array and individual turbine maximizing values of $C'_{T,1}$ differ the most, and this difference decreases with increasing yaw misalignment angles. The efficiency of turbine 1 is shown in figure 9(*b*). As is shown, the array efficiency is maximized at a turbine 1 yaw and thrust that is neither the standard Betz maximum nor the maximum as a function of γ_1 (4.3). While operating turbine 1 at $C'^*_{T,1}(\gamma_1)$ would maximize the turbine 1 power, given the applied yaw misalignment, this operation also results in larger wake
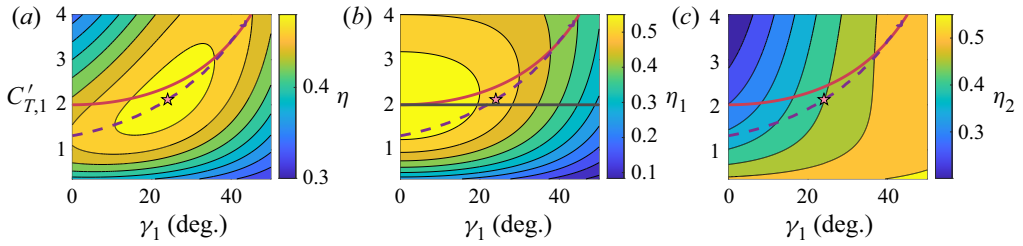
Figure 9. Wake model predictions for (*a*) total wind farm efficiency η, (*b*) freestream individual turbine 1 efficiency, and (*c*) waked individual turbine 2 efficiency. The efficiency is calculated using (4.6). The location of maximum array efficiency (highest total array power output) is indicated with a star symbol. The values of C'_T that maximize the total array power (turbines 1 and 2) for each yaw misalignment angle are shown by the dashed purple line, as predicted empirically from the wake model output. The values of C'_T that maximize the freestream turbine power (turbine 1) for each yaw misalignment angle are shown by the red line, and given as $C'^*_T(\gamma) = 2/\cos^2(\gamma)$. In (*b*), the individual freestream yaw-aligned wind turbine efficiency-maximizing thrust coefficient $C'^*_T(\gamma = 0) = 2$ is shown with a horizontal line.

velocity deficits. The efficiency of turbine 2 depending on γ_1 and $C'_{T,1}$ is shown in figure 9(*c*). The efficiency of turbine 2 increases with increasing turbine 1 yaw or a decreasing turbine 1 thrust coefficient.

In summary, the array efficiency-maximizing operation has a lower value of $C'_{T,1}$ than the value that maximizes the power of turbine 1, in order to increase the power of turbine 2. The operating point of optimal efficiency is a combination of yaw and induction control. At lower yaw values, induction control (reduction in $C'_{T,1}$) is more active. At higher yaw values, the array efficiency is maximized at values of $C'_{T,1}$ that are close to the operation that maximizes the upstream turbine efficiency ($C'^*_{T,1}(\gamma_1) = 2/\cos^2(\gamma_1)$).

The proximity of the optimal operating point to the turbine 1 power-maximizing curve ($C'^*_{T,1}(\gamma_1) = 2/\cos^2(\gamma_1)$) reaffirms that wake steering control is strongly dependent on the power–yaw relationship of the freestream turbine, since the freestream turbines contribute a larger fraction of the total array power (Howland *et al.* 2020*c*, 2022). However, the departure from the curve (i.e. the misalignment of the solid red line and the dashed purple line in figure 9*a*) reaffirms that it is also important to accurately model the wakes and the power of each turbine in the array to locate the array power-maximizing operation. The power-maximizing operation will depend on the wind conditions and the wind farm geometry, necessitating an accurate parametric model that can capture these trends. The model developed in § 2 and used here enables the prediction of the induction, thrust and power of a yaw-misaligned actuator disk, in addition to the velocity deficit initial conditions for far-wake models.

5. Conclusions

The velocity induced by an actuator disk depends jointly on the yaw misalignment angle and the thrust coefficient. This dependence affects the thrust, wake velocity deficit, wake deflection and power production of a yaw-misaligned actuator disk. Therefore, the characteristic reduction in power production associated with wind turbine yaw misalignment depends on the thrust coefficient of the wind turbine. As such, a tuned, empirical cosine model ($P_r = \cos^{P_p}(\gamma)$) for the power–yaw relationship of a wind turbine is inherently turbine model-specific. Specifically, the empirical power–yaw factor P_p can be potentially reasonable only for turbines with the same thrust coefficient, although we

note that the relative error of a cosine-based model increases with increasing yaw angles since the true form of P_r is not exactly a cosine function.

An analytical model for the induction of a yaw-misaligned actuator disk is developed and validated against large eddy simulations of an actuator disk model wind turbine. The model yields improved quantitative predictions of the induction, velocities and power of a yawed actuator disk, compared to existing models, by accounting for the effect of the induction on the wind turbine thrust and the momentum associated with the lateral velocity at the outlet of the streamtube encompassing the disk. We optimize the coefficient of power predicted by the developed model to find the thrust coefficient that maximizes the power production of a yawed actuator disk for each value of the yaw misalignment angle. The optimization results, which are the yawed actuator disk analogue to the classical Betz limit, demonstrate that the thrust coefficient should increase monotonically with an increasing magnitude of yaw misalignment to track the optimal power production ($C_T'^*(\gamma) = 2/\cos^2(\gamma)$), and that the maximum power produced by an individual yaw-misaligned actuator disk is $C_P^*(\gamma) = \frac{16}{27}\cos(\gamma)$.

Finally, the developed induction model is used as an initial condition for a turbulent far-wake model to explore an example, two-turbine wind farm control scenario. The model-predicted combined power production for the two-turbine array is maximized through a combination of yaw (wake steering) and thrust coefficient (induction) control modifications which deviate from the individual turbine power-maximizing operation ($C_T' = 2$, $\gamma = 0°$). The yaw and thrust coefficient of the leading turbine affect its own power production (power–yaw relationship $P_r(\gamma)$) but also affect the wake velocity deficit and wake deflection, which influences the power production of the downwind turbine. The modelling results demonstrate the physical mechanisms for synergistic wake steering and induction, a strategy that has been shown to be effective in previous simulation studies of farm flow control (e.g. Munters & Meyers 2018).

For rotational, utility-scale wind turbines, the realized power–yaw relationship (i.e. $P_r(\gamma)$) will depend on the realized local thrust coefficient C_T' and any potential dependence of C_T' on the yaw misalignment angle. Such a dependence can be integrated into the present modelling framework through the functional form of the thrust force (2.2).

In addition to the effects of the yaw and thrust coefficient on the rotor-averaged induction, yaw misalignment also generates an induced velocity that exhibits spatial variation over the rotor area (Glauert 1926; Hur *et al.* 2019). Since the focus of this study was to predict the rotor-averaged induction and thrust for yaw-misaligned actuator disks, and since the ADM thrust and power depend on the rotor-averaged disk velocity, the azimuthal variations in the induction, which have zero mean (Hur *et al.* 2019), do not affect the proposed model (see § 2). For rotational wind turbine models that distribute thrust unequally in the rotor area, the azimuthal thrust variation is important to model. Future work that focuses on extending the present analysis to rotational wind turbines should consider the effects of spatially variable induction.

Often, numerical implementations of blade-element momentum (BEM) theory predict that the power ratio of a yaw-misaligned wind turbine follows $P_r = \cos^3(\gamma)$ (e.g. Liew *et al.* 2020). Yawed wind turbines, operating with a fixed C_T' in uniform flow, will not have a power ratio $P_r = \cos^3(\gamma)$ since the rotor-normal induction factor is reduced by the yaw misalignment. The power produced by a yaw-misaligned turbine is therefore greater than $P_r = \cos^3(\gamma)$ (i.e. $P_p < 3$), although the particular value of power lost by yaw will depend on C_T'. Future work should incorporate the induction model developed here into BEM solvers. Finally, this study focused on spatially uniform inflow.

Wind speed and direction shear (Howland *et al.* 2020*c*) and wake interactions (Liew *et al.* 2020) affect the power production of yaw-misaligned wind turbines. Future work should consider the effects of wind speed and direction shear on the induced velocity of a yawed actuator disk.

Author ORCIDs.
M.F. Howland https://orcid.org/0000-0002-2878-3874.

Appendix A. Sensitivity of LES ADM induction to numerical set-up

The rotor-normal induction factor a_n for $C_T' = 1.33$ is shown as a function of the yaw misalignment angle γ in figure 10(*a*) for LES cases with (M given by (3.5)) and without ($M = 1$) the disk velocity correction factor M. For the yaw-aligned ADM, the uncorrected disk velocity simulation with a small ADM filter width $\Delta/D = 0.29h/D = 0.032$ approaches the momentum theory estimate $a_n = 0.25$ ($\hat{a}_n(\gamma = 0) = 0.245$). On the other hand, the larger ADM filter width case, $\Delta/D = 3h/(2D)$, results in an underprediction of the momentum theory induction ($\hat{a}_n(\gamma = 0) = 0.220$), even with the disk velocity correction activated. While the smaller ADM filter width reproduces more accurately yaw-aligned momentum theory at the disk, it also introduces numerical oscillations in the wake flow field which can introduce errors in wake analysis. However, the rotor-normal induction, when normalized by the yaw-aligned induction ($a_n(\gamma)/a_n(\gamma = 0)$), shown in figure 10(*b*), demonstrates that the normalized quantities are less sensitive to the numerical set-up. Therefore, in the results in § 4, where analysis of the wake velocity is required (for δu_0 and δv_0) and normalized quantities are presented, we use the disk correction with M given by (3.5) and a larger ADM filter width $\Delta/D = 3h/(2D)$. In § 4, where unnormalized quantities are presented and the wake flow is not analysed, we use a smaller ADM filter width $\Delta/D = 0.29h/D = 0.032$, which reproduces well-accepted momentum theory for the yaw-aligned turbine (see Appendix D) and does not require the disk velocity correction (Shapiro *et al.* 2019*a*).

Appendix B. Glauert induction and power–yaw model

Glauert (1926) developed a model for the relationship between the thrust coefficient C_T and the rotor-averaged induction normal to the rotor a_n^g (see derivation in Burton *et al.* 2011):

$$C_T = 4a_n^g\sqrt{1 - a_n^g(2\cos(\gamma) - a_n^g)}. \tag{B1}$$

Equation (B1) can be solved iteratively for a_n^g given a known C_T from the initial condition of the yaw-aligned induction. The Glauert model for C_P is

$$C_P^g = 4a_n^g\sqrt{1 - a_n^g(2\cos(\gamma) - a_n^g)}\,(\cos(\gamma) - a_n^g), \tag{B2}$$
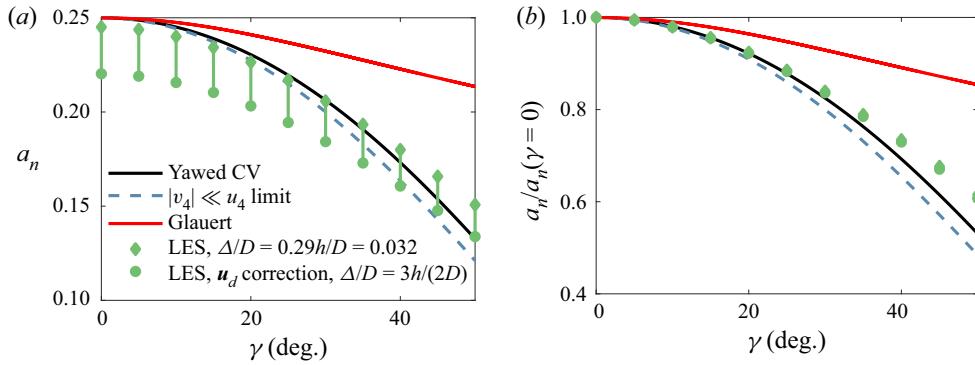
Figure 10. (*a*) Rotor-normal induction for the yawed ADM wind turbine with $C'_T = 1.33$. The LES results are shown with (*M* given by (3.5), $\Delta/D = 3h/(2D)$) and without ($M = 1$, $\Delta/D = 0.29h/D = 0.032$) the disk velocity $\boldsymbol{u}_d$ correction factor. The cases with and without the correction factor use a larger and smaller ADM filter width Δ, respectively. The model predictions are given by the 'Yawed CV' curve, and the limiting case $|v_4| \ll u_4$ is shown. (*b*) Same as (*a*) except the rotor-normal induction values are normalized by the yaw-aligned ADM rotor-normal induction, $a_n(\gamma)/a_n(\gamma = 0)$.

and the Glauert power ratio model is $P_r^g(\gamma) = C_P^g(\gamma)/C_P^g(\gamma = 0)$, where C_P^g is estimated using (B2).

Appendix C. Far-wake model

The inviscid near-wake model developed in §2 can provide the initial conditions for self-similar far-wake models. The streamwise and spanwise velocity initial conditions are u_4 and v_4, respectively (see §2). We use a far-wake model based on the analytical integration of the lifting line model (Shapiro *et al.* 2018) shown in Howland, Lele & Dabiri (2019). The wind turbine wakes are modelled as Gaussian velocity deficits (Bastankhah & Porté-Agel 2014; Shapiro *et al.* 2018; Howland *et al.* 2019). The model is steady-state and neglects wake curling (Howland *et al.* 2016; Martínez-Tossas *et al.* 2021), wind speed shear, wind direction shear and ground effects. We define the upwind turbine with the index *i* and the downwind turbine with the index *j*. The velocity deficit at hub-height associated with an upwind turbine *i* is

$$\mathrm{d}u_i(x, y) = \delta u_i(x) \frac{D^2}{8\sigma_{0,i}^2} \exp\left(-\frac{(y - y_{c,i}(x))^2}{2\sigma_{0,i}^2 d_i^2(x)}\right), \tag{C1}$$

where *D* is the turbine diameter, and the streamwise and spanwise directions are *x* and *y*, respectively. The coordinate system is defined with respect to the position of the upwind turbine *i*, such that the centroid of turbine *i* is at $x = 0$ and $y = 0$. The normalized far-wake diameter as a function of the streamwise location *x* is $d_i(x) = 1 + k_{w,i} \log(1 + \exp[2(x/D - 1)])$. The wake spreading coefficient is k_w, and the proportionality constant of the presumed Gaussian wake is σ_0. The lateral centroid of the wake of turbine *i* is $y_{c,i}$. With freestream wind u_∞ in the *x*-direction and zero freestream wind in the spanwise direction, the streamwise velocity deficit $\delta u_i(x)$ is modelled as (Shapiro *et al.* 2018)

$$\delta u_i(x) = \frac{u_\infty - u_{4,i}}{d_i^2(x)} \frac{1}{2}\left[1 + \mathrm{erf}\left(\frac{x}{\sqrt{2}D/2}\right)\right], \tag{C2}$$

959 A9-21

and the wake centreline lateral velocity as a function of the x-position for the upwind turbine is

$$\delta v_i(x) = \frac{-v_{4,i}}{d_i^2(x)} \frac{1}{2} \left[1 + \mathrm{erf}\left(\frac{x}{\sqrt{2}\, D/2} \right) \right]. \tag{C3}$$

The initial conditions for the far-wake model in (C2) and (C3) are provided by the inviscid model developed in § 2 (u_4 and v_4). The lateral centroid of the wake, produced by upwind turbine i, is given by

$$y_{c,i}(x) = \int_{x_{0,i}}^{x} \frac{-\delta v_i(x')}{u_\infty} \, dx'. \tag{C4}$$

To compute power for an ADM turbine (§ 2.1), we use an estimate of the rotor-averaged velocity in the far-wake model. To result in an analytical expression in a two-dimensional model, we can approximate the surface integral of the Gaussian velocity deficit over the waked rotor as an integral over the diameter in the y-direction at hub-height (C1). The analytical, averaged velocity deficit is (Howland *et al.* 2019)

$$\Delta u_{i,j}(x) = \frac{\sqrt{2\pi}\, \delta u_i(x)\, d_i(x)\, D}{16\sigma_{0,i}} \left[\mathrm{erf}\left(\frac{y_T + D/2 - y_{c,i}(x)}{\sqrt{2}\, \sigma_{0,i}\, d_i(x)} \right) - \mathrm{erf}\left(\frac{y_T - D/2 - y_{c,i}(x)}{\sqrt{2}\, \sigma_{0,i}\, d_i(x)} \right) \right], \tag{C5}$$

where the lateral turbine centroid of downwind turbine j is y_T. More generally, the rotor-averaged velocity deficit can be calculated through numerical integration over y and z using (C1), which affects output power (P_2) and optimal control results by a few per cent (4 % and <0.1 % for γ_1^* and $C_{T,1}^*$, respectively, in § 4.3). The rotor-averaged velocity at the downwind turbine j without induction effects is given by

$$u_{e,j} = u_\infty - \Delta u_{i,j}, \tag{C6}$$

and the power production of turbine j, following (2.16), is

$$P_j = \tfrac{1}{2} \rho C'_{T,j} A_d \left[(1 - a_{n,j}) \cos(\gamma_j)\, u_{e,j} \right]^3. \tag{C7}$$

The power of turbine i is modelled similarly.

Appendix D. Validation of the LES ADM

In this appendix, we validate the LES ADM through comparisons to standard, yaw-aligned ($\gamma = 0$) momentum theory. Yaw-aligned momentum theory results in the following equations for the rotor-normal induction factor, streamwise wake velocity and spanwise wake velocity (e.g. Burton *et al.* 2011):

$$\left. \begin{aligned} a_n(\gamma = 0) = a &= \frac{C'_T}{C'_T + 4} = \frac{1}{2}(1 - \sqrt{1 - C_T}), \\[2mm] \frac{u_4(\gamma = 0)}{u_\infty} &= \frac{4 - C'_T}{4 + C'_T} = 1 - 2a, \\[2mm] \frac{v_4(\gamma = 0)}{u_\infty} &= 0. \end{aligned} \right\} \tag{D1}$$

The corresponding thrust and power coefficients are $C_T = 4a(1 - a)$ and $C_P = 4a(1 - a)^2$, respectively. The predictions from yaw-aligned momentum theory are shown in
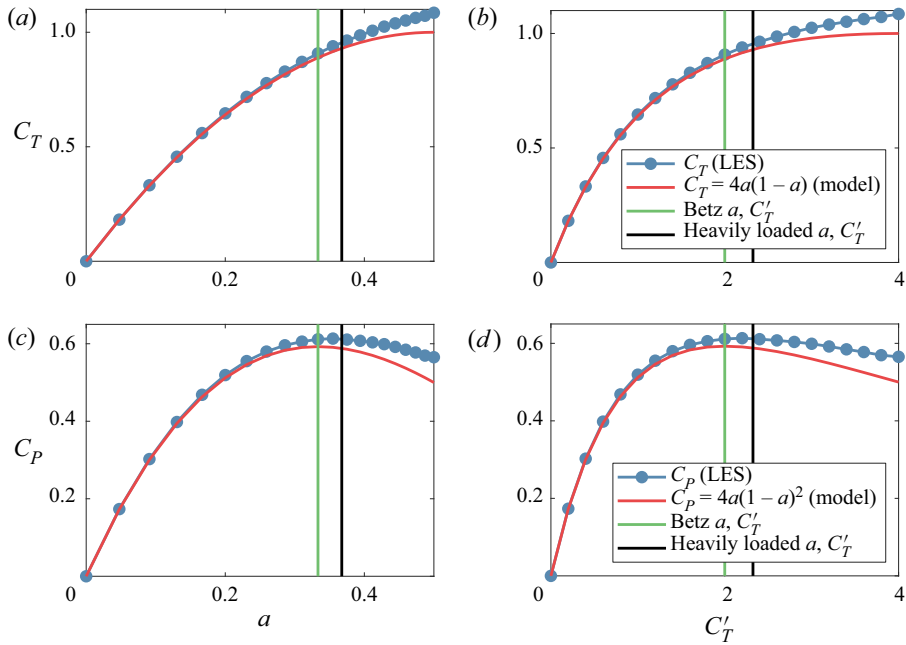
Figure 11. Comparison between yaw-aligned ($\gamma = 0$) momentum theory and LES results for the ADM without the disk velocity $\boldsymbol{u}_d$ correction factor ($M = 1$, $\Delta/D = 0.29h/D = 0.032$). For a yaw-aligned turbine, the rotor-normal induction is $a_n = a$, where a is the standard axial induction factor predicted by momentum theory. Coefficient of thrust C_T is shown as a function of (a) induction factor a, and (b) C_T'. Coefficient of power C_P is shown as a function of (c) induction factor a, and (d) C_T'. The vertical lines report the induction a and thrust coefficient C_T' corresponding to the Betz limit ($a = 1/3$, $C_T' = 2$) and the heavy loading limit ($a = 0.37$, $C_T' = 2.3$) (Wilson & Lissaman 1974; Burton *et al.* 2011).

figure 11, in addition to the LES results ($\gamma = 0$). Induction (C_T') values beyond $a = 0.5$ ($C_T' = 4$) are not shown, as momentum theory predicts negative or zero wake velocity (Burton *et al.* 2011). We additionally show the Betz prediction, which maximizes C_P for $\gamma = 0$ as $a = 1/3$ and $C_T' = 2$. Standard yaw-aligned momentum theory is well-known to have reduced accuracy for increasing values of induction (heavily loaded turbines), due to the flow separation, large pressure drop, and the correspondingly high thrust (Burton *et al.* 2011). Wilson & Lissaman (1974) approximated empirically this heavy loading transition to occur at $a_t = 1 - \frac{1}{2}\sqrt{C_{T,t}} \approx 0.37$, where $C_{T,t} = 1.6$ (Wilson & Lissaman 1974; Burton *et al.* 2011). Vertical lines show a_t and $C_{T,t}'$ in figure 11. The heavy loading transition provides a reasonable approximation for when standard yaw-aligned momentum theory begins to diverge ($a > a_t$), compared to the LES ADM results.

Appendix E. Evaluation of the local thrust coefficient for rotational turbines

The induction model for yawed actuator disks proposed in §2 treats the local thrust coefficient C_T' and the yaw misalignment angle γ as independent input variables. For yaw-aligned rotational turbines, the thrust is determined primarily by the aerodynamics of the turbine blades and the rotor angular velocity Ω (Burton *et al.* 2011). The dependence of the turbine thrust on yaw misalignment for a rotational turbine depends on the control strategy, namely the pitch and torque control (Howland *et al.* 2020c). Therefore, the power loss due to yaw misalignment is both turbine-specific and specific to the control method.
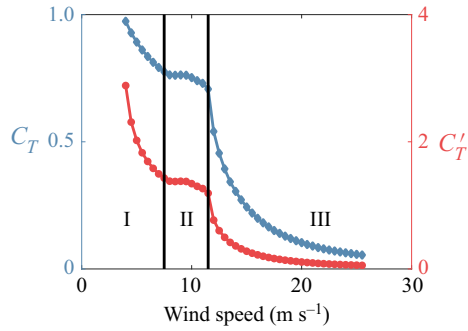
Figure 12. Coefficient of thrust C_T and local coefficient of thrust C'_T for the NREL 5 MW reference turbine (Jonkman *et al.* 2009). Approximate control regions (I, II and III) are identified.

Turbines in standard, yaw-aligned operation aim to maximize power generation in region II. For yaw-aligned (standard) conditions within region II, a rotational turbine keeps the blade pitch angle constant and maintains a constant tip-speed ratio (TSR) $\lambda \equiv \Omega R/u_\infty$. The TSR controls the thrust force for rotational turbines. Therefore, within standard control in region II, the local thrust coefficient C'_T is constant as a function of the wind speed. The dependence of C'_T and the coefficient of thrust $C_T \equiv 2|\boldsymbol{F}_T|/(\rho A_d u_\infty^2)$ is shown in figure 12 for the NREL 5 MW reference turbine (Jonkman *et al.* 2009).

Here, we assess the influence of the control strategy on the relationship between C'_T and the yaw misalignment angle in region II operation. Using experimental data from Krogstad & Adaramola (2012), we show that the qualitative relationship between C'_T and γ changes with different turbine control strategies. Krogstad & Adaramola (2012) measured the coefficient of thrust C_T for a 0.9 m wind turbine model in a wind tunnel, varying yaw misalignment angle and TSR. For a turbine in yaw misalignment, the relationship between the coefficient of thrust C_T and the local thrust coefficient C'_T is given by

$$C_T = C'_T(1 - a_n(\gamma))^2 \cos^2(\gamma), \tag{E1}$$

which can be appended to the proposed model (2.15) and solved iteratively given C_T and γ. We use the proposed model (2.15) to compute C'_T from the C_T measurements of Krogstad & Adaramola (2012).

The local thrust coefficient depends on both the yaw misalignment angle γ and the TSR λ, as shown in figure 13(*a*). We explore two hypothetical control strategies for the angular velocity Ω as a function of yaw γ for a rotational turbine in region II operation. One control strategy maintains a constant TSR such that $\lambda = \Omega R/u_\infty$ is constant regardless of yaw misalignment angle. With this control strategy, increasing the yaw misalignment generally decreases the local thrust coefficient C'_T. This is shown by following the vertical lines in figure 13(*a*) through changing yaw misalignment angle, which is also presented in figure 13(*b*). We then consider a second control strategy in which we hold a modified TSR $\lambda' = (\Omega \cos(\gamma) R)/u_\infty$ constant. This modifies the relationship between local thrust coefficient C'_T and yaw alignment angle γ. For the model turbine used by Krogstad & Adaramola (2012), the effect of the second control strategy (targeting constant λ') is an increase in the local thrust coefficient C'_T relative to the first control strategy targeting constant λ at each yaw value. The optimal operating point that maximizes $C_P(\gamma = 0)$ is $\lambda = 6$ (Krogstad & Adaramola 2012). For $\lambda' = 6$, C'_T is approximately constant as a function of yaw γ (figure 13*b*).
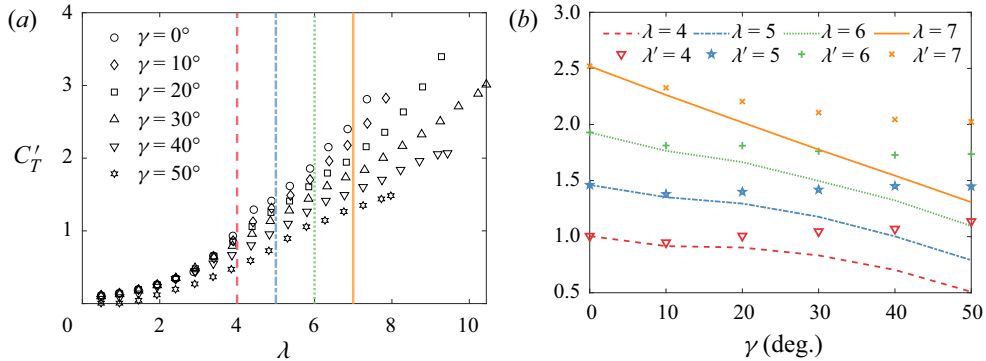
959 A9-24

Figure 13. (*a*) Thrust coefficient C'_T as a function of TSR at various yaw misalignment angles, using C_T data from Krogstad & Adaramola ([2012](#)). The thrust coefficient C'_T is solved for iteratively using the proposed model ([2.15](#)) with ([E1](#)). (*b*) Dependence of the thrust coefficient C'_T on yaw for two different control strategies: constant $\lambda = \Omega R / u_\infty$, and constant $\lambda' = (\Omega \cos(\gamma) R) / u_\infty$.

REFERENCES

AINSLIE, J.F. 1988 Calculating the flowfield in the wake of wind turbines. *J. Wind Engng Ind. Aerodyn.* **27** (1–3), 213–224.

ANNONI, J., GEBRAAD, P.M., SCHOLBROCK, A.K., FLEMING, P.A. & VAN WINGERDEN, J.-W. 2016 Analysis of axial-induction-based wind plant control using an engineering and a high-order wind plant model. *Wind Energy* **19** (6), 1135–1150.

BARTHELMIE, R.J., HANSEN, K., FRANDSEN, S.T., RATHMANN, O., SCHEPERS, J., SCHLEZ, W., PHILLIPS, J., RADOS, K., ZERVOS, A. & POLITIS, E. 2009 Modelling and measuring flow and wind turbine wakes in large wind farms offshore. *Wind Energy* **12** (5), 431–444.

BASTANKHAH, M. & PORTÉ-AGEL, F. 2014 A new analytical model for wind-turbine wakes. *Renew. Energy* **70**, 116–123.

BASTANKHAH, M. & PORTÉ-AGEL, F. 2016 Experimental and theoretical study of wind turbine wakes in yawed conditions. *J. Fluid Mech.* **806**, 506–541.

BASTANKHAH, M. & PORTÉ-AGEL, F. 2019 Wind farm power optimization via yaw angle control: a wind tunnel study. *J. Renew. Sustain. Energy* **11** (2), 023301.

BOERSMA, S., DOEKEMEIJER, B., GEBRAAD, P.M., FLEMING, P.A., ANNONI, J., SCHOLBROCK, A.K., FREDERIK, J. & VAN WINGERDEN, J.-W. 2017 A tutorial on control-oriented modeling and control of wind farms. In *2017 American Control Conference (ACC)*. IEEE.

BURTON, T., JENKINS, N., SHARPE, D. & BOSSANYI, E. 2011 *Wind Energy Handbook*. John Wiley & Sons.

CALAF, M., MENEVEAU, C. & MEYERS, J. 2010 Large eddy simulation study of fully developed wind-turbine array boundary layers. *Phys. Fluids* **22** (1), 015110.

CHOUKULKAR, A., PICHUGINA, Y., CLACK, C.T., CALHOUN, R., BANTA, R., BREWER, A. & HARDESTY, M. 2016 A new formulation for rotor equivalent wind speed for wind resource assessment and wind power forecasting. *Wind Energy* **19** (8), 1439–1452.

DAHLBERG, J. & MONTGOMERIE, B. 2005 Research program of the Utgrunden demonstration offshore wind farm, final report: Part 2, wake effects and other loads. *Rep. FOI*, pp. 2–17. Swedish Defence Research Agency.

FLEMING, P., ANNONI, J., CHURCHFIELD, M., MARTINEZ-TOSSAS, L.A., GRUCHALLA, K., LAWSON, M. & MORIARTY, P. 2018 A simulation study demonstrating the importance of large-scale trailing vortices in wake steering. *Wind Energy Sci.* **3** (1), 243–255.

FLEMING, P., GEBRAAD, P.M., LEE, S., VAN WINGERDEN, J.-W., JOHNSON, K., CHURCHFIELD, M., MICHALAKES, J., SPALART, P. & MORIARTY, P. 2015 Simulation comparison of wake mitigation control strategies for a two-turbine case. *Wind Energy* **18** (12), 2135–2143.

FLEMING, P., KING, J., DYKES, K., SIMLEY, E., ROADMAN, J., SCHOLBROCK, A., MURPHY, P., LUNDQUIST, J.K., MORIARTY, P., FLEMING, K., *et al.* 2019 Initial results from a field campaign of wake steering applied at a commercial wind farm – Part 1. *Wind Energy Sci.* **4** (2), 273–285.

Frandsen, S., Barthelmie, R., Pryor, S., Rathmann, O., Larsen, S., Højstrup, J. & Thøgersen, M. 2006 Analytical modelling of wind speed deficit in large offshore wind farms. *Wind Energy* **9** (1–2), 39–53.

Gebraad, P., Teeuwisse, F., Van Wingerden, J., Fleming, P.A., Ruben, S., Marden, J. & Pao, L. 2016 Wind plant power optimization through yaw control using a parametric model for wake effects – a CFD simulation study. *Wind Energy* **19** (1), 95–114.

Ghate, A.S. & Lele, S.K. 2017 Subfilter-scale enrichment of planetary boundary layer large eddy simulation using discrete Fourier–Gabor modes. *J. Fluid Mech.* **819**, 494–539.

Glauert, H. 1926 A general theory of the autogyro. *Tech. Rep.* 1111. HM Stationery Office.

Gottlieb, S., Ketcheson, D.I. & Shu, C.-W. 2011 *Strong Stability Preserving Runge–Kutta and Multistep Time Discretizations*. World Scientific.

Hansen, M. 2015 *Aerodynamics of Wind Turbines*. Routledge.

Howland, M.F., Bossuyt, J., Martínez-Tossas, L.A., Meyers, J. & Meneveau, C. 2016 Wake structure in actuator disk models of wind turbines in yaw under uniform inflow conditions. *J. Renew. Sustain. Energy* **8** (4), 043301.

Howland, M.F., Ghate, A.S. & Lele, S.K. 2020*a* Influence of the geostrophic wind direction on the atmospheric boundary layer flow. *J. Fluid Mech.* **883**, A39.

Howland, M.F., Ghate, A.S., Lele, S.K. & Dabiri, J.O. 2020*b* Optimal closed-loop wake steering – Part 1: conventionally neutral atmospheric boundary layer conditions. *Wind Energy Sci.* **5** (4), 1315–1338.

Howland, M.F., Ghate, A.S., Quesada, J.B., Pena Martínez, J.J., Zhong, W., Larrañaga, F.P., Lele, S.K. & Dabiri, J.O. 2022*a* Optimal closed-loop wake steering – Part 2: diurnal cycle atmospheric boundary layer conditions. *Wind Energy Sci.* **7** (1), 345–365.

Howland, M.F., González, C.M., Martínez, J.J.P., Quesada, J.B., Larranaga, F.P., Yadav, N.K., Chawla, J.S. & Dabiri, J.O. 2020*c* Influence of atmospheric conditions on the power production of utility-scale wind turbines in yaw misalignment. *J. Renew. Sustain. Energy* **12** (6), 063307.

Howland, M.F., Lele, S.K. & Dabiri, J.O. 2019 Wind farm power optimization through wake steering. *Proc. Natl Acad. Sci. USA* **116** (29), 14495–14500.

Howland, M.F., Quesada, J.B., Martinez, J.J.P., Larrañaga, F.P., Yadav, N., Chawla, J.S., Sivaram, V. & Dabiri, J.O. 2022*b* Collective wind farm operation based on a predictive model increases utility-scale energy production. *Nat. Energy* **7**, 818–827.

Hur, C., Berdowski, T., Simao Ferreira, C., Boorsma, K. & Schepers, G. 2019 A review of momentum models for the actuator disk in yaw. *AIAA Paper* 2019-1799.

Jiménez, A., Crespo, Á. & Migoya, E. 2010 Application of a LES technique to characterize the wake deflection of a wind turbine in yaw. *Wind Energy* **13** (6), 559–572.

Jonkman, J., Butterfield, S., Musial, W. & Scott, G. 2009 Definition of a 5-MW reference wind turbine for offshore system development. *Tech. Rep.* NREL/TP-500-38060. National Renewable Energy Laboratory.

Jonkman, J.M. & Buhl, M.L. 2005 FAST user's guide. *Tech. Rep.* NREL/EL-500-38230. National Renewable Energy Laboratory.

Kheirabadi, A.C. & Nagamune, R. 2019 A quantitative review of wind farm control with the objective of wind farm power maximization. *J. Wind Engng Ind. Aerodyn.* **192**, 45–73.

Krogstad, P.-r. & Adaramola, M.S. 2012 Performance and near wake measurements of a model horizontal axis wind turbine. *Wind Energy* **15** (5), 743–756.

Liew, J.Y., Urbán, A.M. & Andersen, S.J. 2020 Analytical model for the power–yaw sensitivity of wind turbines operating in full wake. *Wind Energy Sci.* **5** (1), 427–437.

Martínez-Tossas, L.A., Churchfield, M.J. & Leonardi, S. 2015 Large eddy simulations of the flow past wind turbines: actuator line and disk modeling. *Wind Energy* **18** (6), 1047–1060.

Martínez-Tossas, L.A., King, J., Quon, E., Bay, C.J., Mudafort, R., Hamilton, N., Howland, M.F. & Fleming, P.A. 2021 The curled wake model: a three-dimensional and extremely fast steady-state wake solver for wind plant flows. *Wind Energy Sci.* **6** (2), 555–570.

Micallef, D. & Sant, T. 2016 A review of wind turbine yaw aerodynamics. In *Wind Turbines – Design, Control and Applications* (ed. A.G. Aissaoui & A. Tahour), chap. 2, pp. 27–54. InTechOpen.

Milne-Thomson, L.M. 1973 *Theoretical Aerodynamics*. Courier Corporation.

Munters, W. & Meyers, J. 2017 An optimal control framework for dynamic induction control of wind farms and their interaction with the atmospheric boundary layer. *Phil. Trans. R. Soc. Lond.* A **375** (2091), 20160100.

Munters, W. & Meyers, J. 2018 Dynamic strategies for yaw and induction control of wind farms based on large-eddy simulation and optimization. *Energies* **11** (1), 177.

NAGARAJAN, S., LELE, S.K. & FERZIGER, J.H. 2003 A robust high-order compact method for large eddy simulation. *J. Comput. Phys.* **191** (2), 392–419.

NICOUD, F., TODA, H.B., CABRIT, O., BOSE, S. & LEE, J. 2011 Using singular values to build a subgrid-scale model for large eddy simulations. *Phys. Fluids* **23** (8), 085106.

NORDSTRÖM, J., NORDIN, N. & HENNINGSON, D. 1999 The fringe region technique and the Fourier method used in the direct numerical simulation of spatially evolving viscous flows. *SIAM J. Sci. Comput.* **20** (4), 1365–1393.

PAO, L.Y. & JOHNSON, K.E. 2009 A tutorial on the dynamics and control of wind turbines and wind farms. In *2009 American Control Conference*, pp. 2076–2089. IEEE.

SCHREIBER, J., NANOS, E., CAMPAGNOLO, F. & BOTTASSO, C.L. 2017 Verification and calibration of a reduced order wind farm model by wind tunnel experiments. *J. Phys.: Conf. Ser.* **854**, 012041.

SHAPIRO, C.R., GAYME, D.F. & MENEVEAU, C. 2018 Modelling yawed wind turbine wakes: a lifting line approach. *J. Fluid Mech.* **841**, R1.

SHAPIRO, C.R., GAYME, D.F. & MENEVEAU, C. 2019*a* Filtered actuator disks: theory and application to wind turbine models in large eddy simulation. *Wind Energy* **22** (10), 1414–1420.

SHAPIRO, C.R., STARKE, G.M., MENEVEAU, C. & GAYME, D.F. 2019*b* A wake modeling paradigm for wind farm design and control. *Energies* **12** (15), 2956.

SØRENSEN, J.N. 2011 Aerodynamic aspects of wind energy conversion. *Annu. Rev. Fluid Mech.* **43** (1), 427–448.

SPEAKMAN, G.A., ABKAR, M., MARTÍNEZ-TOSSAS, L.A. & BASTANKHAH, M. 2021 Wake steering of multirotor wind turbines. *Wind Energy* **24** (11), 1294–1314.

STEVENS, R.J., GAYME, D.F. & MENEVEAU, C. 2015 Coupled wake boundary layer model of wind-farms. *J. Renew. Sustain. Energy* **7** (2), 023115.

WILSON, R.E. & LISSAMAN, P. 1974 *Applied Aerodynamics of Wind Power Machines*. Oregon State University.

ZONG, H. & PORTÉ-AGEL, F. 2021 Experimental investigation and analytical modelling of active yaw control for wind farm power optimization. *Renew. Energy* **170**, 1228–1244.